Eur. Phys. J. E (2014) **37**: 41
DOI 10.1140/epje/i2014-14041-2

THE EUROPEAN PHYSICAL JOURNAL E

Regular Article

# Morphology and growth of polarized tissues

C. Blanch-Mercader[1,2,a], J. Casademunt[1], and J.F. Joanny[2]

[1] Departament d'ECM, Universitat de Barcelona, Avinguda Diagonal 647, E-08028 Barcelona, Spain
[2] Institut Curie, UMR 168, 26 rue d'Ulm, 75005 Paris, France

Received 17 February 2014 and Received in final form 28 March 2014
Published online: 26 May 2014 – 

**Abstract.** We study and classify the time-dependent morphologies of polarized tissues subject to anisotropic but spatially homogeneous growth. Extending previous studies, we model the tissue as a fluid, and discuss the interplay of the active stresses generated by the anisotropic cell division and three types of passive mechanical forces: viscous stresses, friction with the environment and tension at the tissue boundary. The morphology dynamics is formulated as a free-boundary problem, and conformal mapping techniques are used to solve the evolution numerically. We combine analytical and numerical results to elucidate how the different passive forces compete with the active stresses to shape the tissue in different temporal regimes and derive the corresponding scaling laws. We show that in general the aspect ratio of elongated tissues is non-monotonic in time, eventually recovering isotropic shapes in the presence of friction forces, which are asymptotically dominant.

## 1 Introduction

The regulation of the growth and shape of tissues is a fundamental property of living organisms. The recent development of new experimental techniques has thrown light on the role of force generation at the cellular scale in tissue morphogenesis. For example, cells can reorganize collectively inducing local deformations and forces, which can be isotropically or anisotropically distributed, by cell division and cell apoptosis [1,2]. Reciprocally, the biophysical properties of the tissue can alter the state of the cells. Therefore, it is relevant to study the mechanisms that control cell organization and shape tissues [3–5]. Cell orientation is essential for tissue elongation. For example, in the case of plants it has been shown that the cortical array of microtubules set a preferential direction for cell growth [6–8]. Another example is the wing disk of the fruit fly Drosophila in which gradients of morphogens are responsible for the determination of a macroscopic orientation [3,9]. In this article we focus on the deformations induced at the scale of the tissue shape by oriented cell division. This mechanism requires two essential ingredients: cell replication coupled to a global polarization of the system [10]. The forces produced by this mechanism in general are anisotropically distributed.

The inclusion of growth in continuum models of elastic tissues has been discussed and applied by several authors [11–13]. However, it has been shown that at sufficiently long time scales, a hydrodynamical description of a growing tissue as a viscous fluid is justified [10,14,15]. Our model here extends the approach of ref. [14]. The constitutive equations of the tissue are similar to those of an active nematic fluid [16,17]. Cell division is an active process, in the sense that it requires a consumption of chemical energy. It is taken into account both as a source of matter and as an active local stress. Most of our discussion deals with confluent tissue layers on a substrate.

This article is organized as follows: In the first section we present the model and discuss the underlying hypotheses. We then study the dynamics of the small deformations of an initially circular tissue. In the second and third sections, we extend our results to larger deformations in two regimes, either the dissipation during growth is dominated by friction on the substrate or by tissue viscosity, respectively.

## 2 Physical model

We aim at describing the time evolution of a tissue with an arbitrary initial shape and a spatially uniform rate of expansion. The model is an extension of a previous continuum approach for polarized tissues discussed in refs. [9, 14], including additional forces that compete with the active stresses, such as friction forces with the environment and effective surface tension at the tissue boundary.

Our physical description is given in terms of the macroscopic fields: the cell density $\rho$, the cell velocity $\mathbf{v}$, the local cell orientation characterized by a unit vector $\mathbf{p}$, the total internal stresses $\sigma^{\mathrm{tot}}_{\alpha\beta}$ and the pressure field $P$. In

[a] e-mail: cblanchme@gmail.com

this coarse-grained description, the macroscopic fields are assumed to be averaged over a small region comprising several cells.

The cell number balance equation includes a source term which accounts for the increment in cell number due to proliferation and the decrease of cell number due to cell death. We write it as

$$\partial_t \rho + \partial_\alpha(\rho v_\alpha) = k_c \rho, \tag{1}$$

where Greek indices denote Cartesian coordinates and we adopt Einstein's summation convention over Greek indices. The growth rate $k_c > 0$ is the difference between cell division and cell death rates. For simplicity we also assume that the tissue is incompressible so that the cell density $\rho$ is assumed to be constant.

Our focus on long time scales, such that local cell rearrangements and cell proliferation and cell death events lead to an effective fluid-like behavior of the tissue [10,14, 15]. Furthermore, a growing tissue must be considered as an active material because cell division is an active process, which requires a continuous consumption of chemical energy [17]. In this paper we study polarized tissues where the cells have a well-defined orientation ($\mathbf{p}$), which we may assume to be fixed by an external field such as a morphogen gradient. Consequently, we treat the tissue as an active nematic fluid. The constitutive equation for the total stress in an active nematic fluids is discussed in refs. [16,17] and reads

$$\sigma^{\rm tot}_{\alpha\beta} = \eta(\partial_\alpha v_\beta + \partial_\beta v_\alpha) - P\delta_{\alpha\beta} - \sigma_0 p_\alpha p_\beta, \tag{2}$$

where $\eta$ is the shear viscosity. The last term on the right-hand side is the anisotropic active stress. It exists for symmetry reasons, if the tissue has a macroscopic nematic order, and reflects that the active (energy consuming) process of cell division is spatially oriented. Its amplitude $\sigma_0$ is a phenomenological parameter. In principle, within a linear theory the contribution of cell division/death to the active stress should be proportional to the growth rate (*i.e.* $\sigma_0 \propto k_c$). However, there may be other contributions to $\sigma_0$ due to, for example, the activity of the individual cells, which consume ATP. A detailed explanation of the origin of active stresses in a growing tissue can be found in ref. [10]. Note that for tissues growing in two dimensions that we mostly study below, the case where $\sigma_0 > 0$ and $\mathbf{p}$ points in a given direction is equivalent to the case where $\sigma_0 < 0$ and $\mathbf{p}$ point in the perpendicular direction. Without loss of generality, in the following we assume $\sigma_0 > 0$.

When writing the force balance in the tissue, we include an internal viscous drag force proportional to the local velocity field. In a 2-dimensional tissue, growing on a solid substrate to which it is weakly attached by transmembrane proteins, the drag force may be due to the relative movement between the tissue and the substrate. On the other hand, for a tissue growing in a 3-dimensional space, the drag force could be due to the permeation of an external medium through the tissue [18]. It is worth mentioning that both mechanisms are fundamentally different. Neglecting inertia, conservation of momentum can be written as

$$\partial_\alpha \sigma^{\rm tot}_{\alpha\beta} - \xi v_\beta = 0,$$

where $\xi$ is the friction coefficient per unit area or per unit volume.

In order to simplify the model, we consider that $\mathbf{p}$, $k_c$, $\eta$, $\sigma_0$ and $\xi$ are spatially uniform. Furthermore, without loss of generality we choose the coordinates system such that the polarization $\mathbf{p}$ is parallel to the $x$-axis. Therefore, the two coupled equations describing the growth of the tissue are

$$\eta \Delta \mathbf{v} - \boldsymbol{\nabla} P = \xi \mathbf{v}, \tag{3}$$

$$\boldsymbol{\nabla} \cdot \mathbf{v} = k_c. \tag{4}$$

It has been argued by several authors that surface effects in a tissue can be described in terms of an effective surface tension [19]. We consider here that the surface tension $\gamma > 0$ is isotropic and we write a mechanical boundary condition at the surface of the tissue ($\partial\Omega$) of the form

$$\sigma^{\rm tot}_{\alpha\beta} \hat{n}_\beta|_{\partial\Omega} = -\gamma\kappa\hat{n}_\alpha, \tag{5}$$

where $\kappa$ denotes the local total curvature of the interface and $\hat{n}$ is the normal vector at the interface pointing outwards. This form imposes vanishing tangential stresses and the Young-Laplace pressure drop condition, assuming a constant external pressure, and therefore neglecting the viscosity of the outer fluid. Note that the active stresses do not show up explicitly in the bulk equations (3), (4), but are introduced through the boundary condition eq. (5). The evolution of the tissue shape can then be described as the evolution of its boundary, which is determined by the continuity condition at the boundary

$$V_n = \mathbf{v} \cdot \hat{n}|_{\partial\Omega}, \tag{6}$$

where $V_n$ is the normal component of the boundary velocity given by the value of $\mathbf{v}$ from eqs. (3), (4), (5), at the boundary. The dynamics of the tissue is thus formulated as a free-boundary problem.

Some integral properties of the dynamics can be derived exactly for any shape of the tissue and arbitrary parameter values. The simplest ones are obtained in appendix A. The first global property states that the total area (volume) of the tissue grows exponentially regardless of the shape, with $A = A_0 \exp(k_c t)$ ($\mathcal{V} = \mathcal{V}_0 \exp(k_c t)$). This result reflects the fact that we neglect any dependence of the growth rate on stress. Another remarkable exact result is that, under the assumptions of our model and regardless of the shape, the center of mass of the tissue cannot move. This point is not trivial since, in the presence of friction forces, the motion of the center of mass of an active polar fluid can be triggered by morphological symmetry breaking of the boundary [20].

The relative importance of the three different types of passive stresses in the problem depends on the spatial scale considered. Capillary stresses are generically dominant for a small tissue, with high curvature and small velocities. In the opposite limit, for a large tissue, with large velocities, friction forces dominate. Viscous stresses are typically

most relevant at intermediate scales. The material parameters of the tissue define three intrinsic length scales that control the crossover between these regimes. The capillary length $L_c \equiv \gamma/(\eta k_c)$ defines the crossover scale between capillary forces, dominant for smaller scales, to viscous forces at larger scales. Similarly, we define a friction length $L_\eta \equiv \sqrt{\eta/\xi}$ as the scale where viscous and friction forces are comparable. At length scales smaller than $L_\eta$ viscous stresses dominate the dissipation while at length scales larger than $L_\eta$ friction dominates the dissipation. The combination of these two lengths defines yet another length scale as $L_\xi \equiv (L_c L_\eta^2)^{1/3} = (\gamma/(k_c\xi))^{1/3}$, which compares capillary against friction forces. The orders of magnitude of these length scales for a 2-dimensional tissue are $L_\eta \sim 10$–$100\,\mu$m and $L_c \sim 1$–$100\,\mu$m, for typical values of the friction coefficient $\xi \sim 10^3\,\mathrm{Pa\,s}/\mu\mathrm{m}^2$, the growth rate $k_c \sim 1/\mathrm{day}$, the surface tension $\gamma \sim 100\,\mathrm{Pa}\,\mu$m and the shear viscosity $\eta \sim 10^5$–$10^7\,\mathrm{Pa\,s}$, respectively [9,21, 22]. Consequently, $L_\xi \sim 10$–$100\,\mu$m.

In the following, unless explicitly stated, we focus only on the study of 2-dimensional tissues growing on a solid substrate.

### 2.1 Linear perturbation analysis of the circular shape

We consider first a tissue spreading in 2 dimensions with a circular shape and a radius $R(t)$ in the absence of active stresses (*i.e.* $\sigma_0 = 0$). Cells are constantly produced at a rate $k_c$ and the constraint of constant density imposes a radial flow of cells toward the periphery, which drives the expansion of the tissue. By solving eq. (4), we obtain the radial flow field at position $\mathbf{r}$, $\mathbf{v}_0 = (k_c/2)\mathbf{r}$, where the origin is chosen at the center of the tissue. Using the force balance equation (3), and the Young-Laplace law eq. (5) one can calculate the pressure field induced by the friction forces (there is no viscous contribution in this case). Therefore, the pressure field results in $P_0(r,t) = -\xi k_c(r^2 - R(t)^2)/4 + \eta k_c + \gamma/R(t)$. The size of the tissue grows exponentially: $\dot{R}(t) = k_c R(t)/2$. In the absence of active stresses, an initially disk-shaped tissue remains thus circular and increases its area exponentially over time. Importantly, if $\gamma = 0$ and $\xi = 0$, this uniform exponential growth is also exact for any arbitrary shape. The tissue has a self-similar growth with a uniform scale factor that grows exponentially in time (see appendix B for details).

We now consider that the amplitude of the active stress $\sigma_0$ is finite but of order $\epsilon \ll 1$. In order to quantify the anisotropy of the tissue, we use the aspect ratio $H$, defined as the ratio between the major and minor axes. Taking a circular tissue with radius $R(t)$ as an initial state, we perform a linear perturbation analysis in $\epsilon$ to follow the interfacial dynamics. The position of the edge of the perturbed tissue would be given in polar coordinates by $r(\theta,t) = R(t) + a_2(t)\cos(2\theta)$, where $a_2(t)$ is of order $\sigma_0$, and $\theta$ is the polar angle. The perturbation analysis is rather heavy and it is detailed in appendix C. We only discuss here the relevant asymptotic limiting cases. In order to make the discussion clearer, we give in fig. 1 a

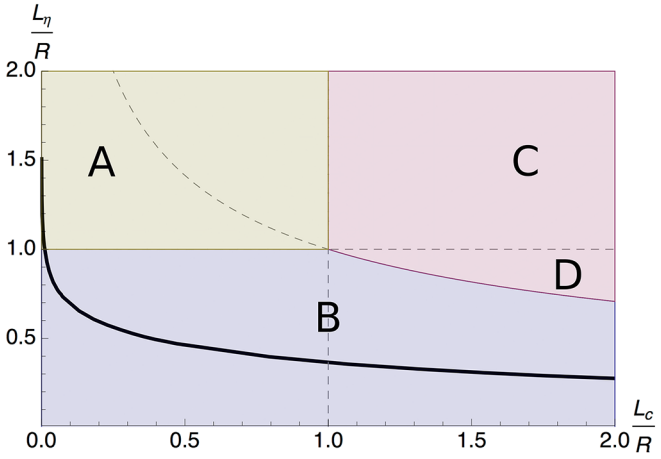


**Fig. 1.** Diagram of states subdivided into the three regions of dominance of passive forces: viscous (yellow), capillary (red) and friction (blue). $R$ is the instantaneous radius of the tissue. The boundaries of the various regimes are defined as $R = L_c$, $R = L_\eta$ and $R = L_\xi$ and the dashed curves are the extension of these boundaries. The transition between regions $C$ and $D$ occurs for $R = L_\eta$. The solid black curve marks the points where the aspect ratio attains its maximum value, for initial radius $R_0 \to 0$, that is, the envelope curve in fig. 2b (gray triangle line). For finite $R_0$ the points of maximal aspect ratio occur below this curve, essentially always in region $B$.

diagram of states of the tissue where the coordinates are $L_c/R(t)$ and $L_\eta/R(t)$. Four asymptotic regions are distinguished in this diagram according to the relative values of the various intrinsic length scales of the problem.

In region $A$ where $L_\eta \gg R \gg L_\xi$, viscous forces dominate the dissipation in the tissue and balance the active stress. In this regime, the aspect ratio satisfies

$$\frac{\mathrm{d}H}{\mathrm{d}t} \approx -\frac{k_c\xi R^2}{6\eta}(H-1) + \frac{\sigma_0}{2\eta}\,. \tag{7}$$

The aspect ratio grows essentially linearly with time in this region and the shape of the tissue becomes anisotropic. In the limit $\xi = 0$, we recover the linear approximation of the case studied in ref. [14], where the aspect ratio grows exponentially in time.

In region $B$ where $R \gg L_\eta, L_\xi$, the dissipation is dominated by the friction forces. The aspect ratio satisfies

$$\frac{\mathrm{d}H}{\mathrm{d}t} \approx -k_c\,(H-1) + \frac{4\sigma_0}{\xi R^2}\,. \tag{8}$$

Eventually, at long times, any tissue enters into this regime where the aspect ratio relaxes to one regardless of its initial morphology, and reaches a circular shape assymptotically. This implies that if the initial morphology of the tissue is circular, the aspect ratio increases from one and reaches a maximum before relaxing back to one.

In the two other regions $C$ and $D$, the variation of the aspect ratio is dominated by capillary forces and surface tension drives the tissue to isotropic circular shapes. In region $C$ where $L_\eta, L_\xi \gg R$ the dissipation is dominated by viscous effects and in addition to the cell division time

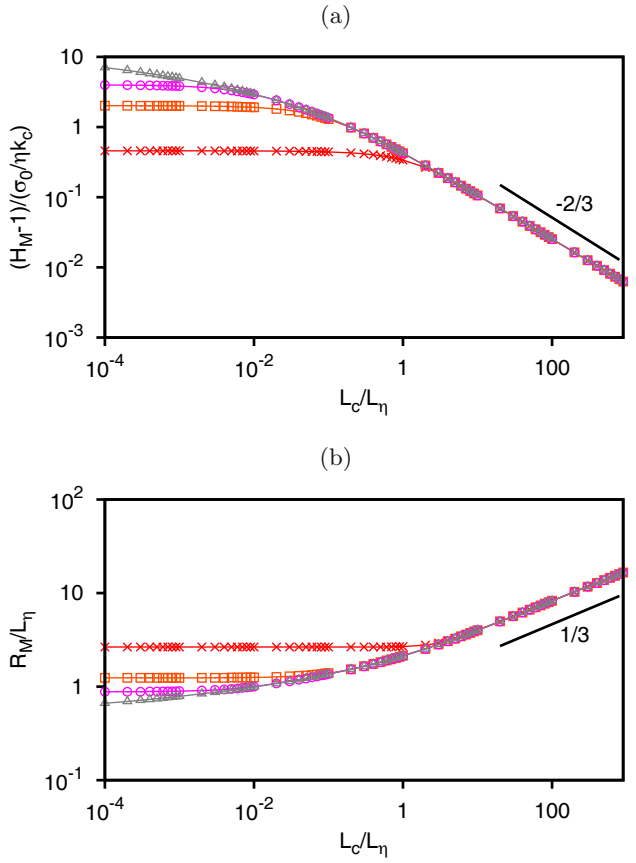


**Fig. 2.** (a) $H_M$ as a function of $L_c/L_\eta$ for different values of $R_0$, $R_0/L_\eta$: 1 (red cross), 0.1 (orange square), 0.01 (pink circle) and 0.0001 (gray triangle). (b) $R_M$ as a function of $L_c/L_\eta$ using the same color code.

there is a second capillary relaxation time $\propto \eta R/\gamma$. The aspect ratio varies according to

$$\frac{\mathrm{d}H}{\mathrm{d}t} \approx -\frac{\gamma}{\eta R}(H-1) + \frac{\sigma_0}{2\eta}. \tag{9}$$

In region $D$ where $L_\xi \gg R \gg L_\eta$, the dissipation is dominated by friction and the capillary relaxation time is $\propto \xi R^3/\gamma$. The aspect ratio varies according to

$$\frac{\mathrm{d}H}{\mathrm{d}t} \approx -\frac{6\gamma}{\xi R^3}(H-1) + \frac{4\sigma_0}{\xi R^2}. \tag{10}$$

In order to characterize the anisotropy of a growing tissue, from now on, we focus on the evolution of initially circular shapes (*i.e.* $H(t=0)=1$) and denote by $R_0$ the initial radius. We solve numerically the general equations obtained in appendix C (C.5), (C.6) for the aspect ratio at linear order in the deviation from the circular shape, assuming that the active stress $\sigma_0$ is small. In general, the aspect ratio $H(t)$ has a maximum at finite time. We define $H_M(L_c, L_\eta, R_0, \sigma_0/\eta k_c)$ as the maximum aspect ratio during a dynamical evolution and $R_M(L_c, L_\eta, R_0, \sigma_0/\eta k_c)$ as the radius at which the aspect ratio is maximal. As shown in fig. 2, $H_M$ is larger for smaller initial radius.

## 3 Friction-dominated growth

In this section we study in more detail the friction regime in which viscous forces are neglected, corresponding to regions $B$ and $D$. In order to do so, we implement a numerical scheme based on the conformal mapping formulation derived in appendix D which allows to compute the evolution of the shape from an arbitrary initial condition, and therefore to go beyond the linear regime discussed in the previous section. Conformal mapping techniques provide a powerful framework to deal with free-boundary Laplacian problems in 2D, in particular to allow for analytical insights, such as shown in appendix E. The connection of the friction-dominated regime to similar problems of Laplacian growth is discussed in appendices D and E.

If $R$ is the average radius of an almost circular tissue, the friction regime is defined by $R \gg L_\eta$. In this case we approximate the original physical model for tissue growth by an incompressible Darcy flow combined with the stress-free boundary condition

$$-\boldsymbol{\nabla} P = \xi \mathbf{v}, \tag{11}$$

$$\boldsymbol{\nabla} \cdot \mathbf{v} = k_c, \tag{12}$$

$$P|_{\partial\Omega} = \gamma\kappa - \sigma_0 \hat{n}_x^2. \tag{13}$$

The active stress produces an anisotropic force on the edge of the tissue.

The morphodynamics in the friction-dominated regime can be understood qualitatively as follows. For $R \ll L_\xi$, capillary forces are dominant and therefore the interface relaxes to mechanical equilibrium faster than it grows (eq. (10)). Consequently the morphology of the tissue evolves in a quasi-static manner such that the aspect ratio increases. On the contrary if $R \gg L_\xi$, friction forces tend to suppress the effects of the active stresses on the

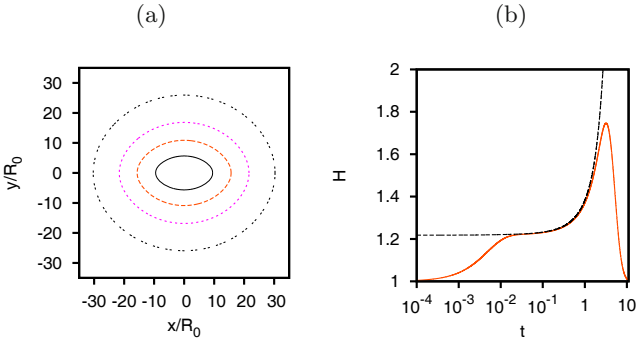


**Fig. 3.** Friction-dominated growth. (a) Temporal evolution of the shape of an initially circular tissue with $R_0 = 0.3$ and $\gamma = 1$, where we show the decrease of the aspect ratio at late stages. The color code stands for $t = 4$ (solid black), $t = 5$ (punctuated orange), $t = 6$ (dotted pink) and $t = 6.5$ (patterned gray). (b) The solid red curve is the temporal evolution of the aspect ratio for the left-hand side case. The dashed black curve is eq. (E.6) for $\gamma = 1$ and the corresponding perimeters at each instant of time of the left-hand side case. Both figures are in units of $\sigma_0/2 = \xi = k_c = 1$.

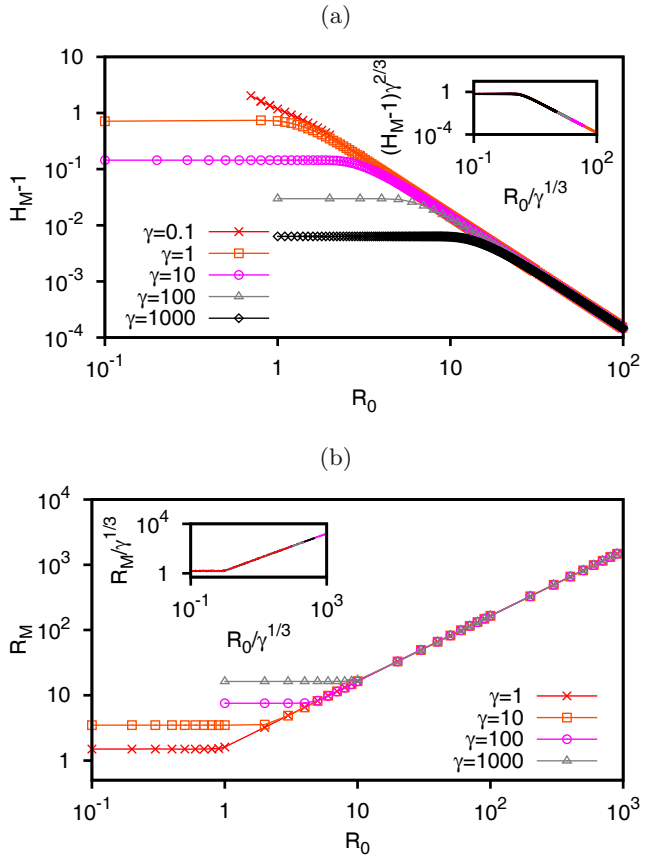


**Fig. 4.** Friction-dominated growth. (a) Maximum aspect ratio ($H_M$) as a function the initial radius $R_0$. Inset: Master curve obtained by rescaling the radius by $L_\xi$ and the aspect ratio by $\gamma^{2/3}$. (b) Radius at which the aspect ratio is maximal ($R_M$), as a function of the initial radius $R_0$ for various values of the surface tension $\gamma$. Inset: Master curve obtained by rescaling the lengths by $L_\xi$. Both figures are in units of $\sigma_0/2 = \xi = k_c = 1$.

morphology (eq. (8)) and consequently the aspect ratio of the tissue decreases upon growth. In fig. 3, we show a typical dynamical evolution of the shape and of the aspect ratio. As in the previous section, the aspect ratio shows a maximum $H_M$ at a finite area ($\equiv \pi R_M^2$).

The quasi-static growth of the regime $R \ll L_\xi$ can be described analytically in more detail. In appendix E we discuss a family of non-trivial shapes for which the active stresses balance exactly the surface tension, when the growth rate can be taken as vanishingly small. The evolution in this early regime is expected to follow quasi-statically the corresponding sequence of shapes within this family, as shown in fig. 3b.

In fig. 4, we plot both the maximum aspect ratio $H_M$ and the corresponding radius $R_M$ as a function of the initial radius $R_0$. For both curves, there are clearly two regions separated by a single length scale which is proportional to the length $L_\xi = (\gamma/(\xi k_c))^{1/3}$, which compares the capillary forces against friction forces.

We now give a simple scaling analysis based on the perturbation equations (8), (10). For $R_0 \ll L_\xi$, the aspect ratio evolves quasi-statically as $H(t) - 1 \propto \sigma_0 R(t)/\gamma$, whereas in the large size limit the aspect ratio decays as $H(t) - 1 \propto \sigma_0/(\xi k_c R(t)^2)$. Therefore by matching these two behaviors, we find that the size at which they coincide and the maximal aspect ratio scale as

$$R_M \propto \left(\frac{\gamma}{\xi k_c}\right)^{1/3} = L_\xi, \tag{14}$$

$$H_M - 1 \propto \frac{\sigma_0}{(\gamma^2 \xi k_c)^{1/3}}, \tag{15}$$

regardless of the initial size $R_0$.

On the contrary, if $R_0 \gg L_\xi$, the system is already in the large size limit so $H(t) - 1 \propto \sigma_0/(\xi k_c R(t)^2)$, and the maximum aspect ratio is reached for a radius proportional to $R_0$. In this limit, we therefore obtain the following scaling:

$$R_M \propto R_0, \tag{16}$$

$$H_M - 1 \propto \frac{\sigma_0}{\xi k_c R_0^2}. \tag{17}$$

In the inset of fig. 4, we rescale the axis to obtain master curves for $R_M$ and $H_M$ showing that our numerical results satisfy these scaling laws.

## 4 Viscosity-dominated growth

Finally we extend our discussion of the viscous regime defined by $R \ll L_\eta$, corresponding to regions $A$ and $C$ by using conformal mapping techniques detailed in appendix F. In this regime, only viscous and capillary forces are considered. The ratio between these two forces defines the capillary length scale $L_c$. Contrary to the friction-dominated regime (*i.e.* $R \gg L_\eta$), the shape anisotropy grows monotonically over time (fig. 5) because neither the capillary force nor the viscous force can counterbalance the active stresses. Nevertheless the interface dynamics depends on

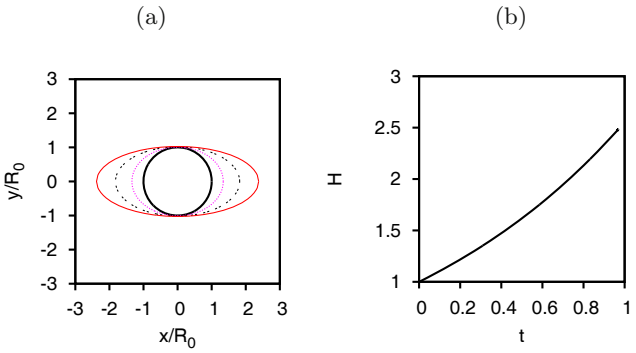


**Fig. 5.** Viscosity-dominated growth. (a) Temporal evolution of the shape of an initially circular tissue with $R_0 = 10$ and $\sigma_0 = 1$. The color code stands for $t = 0$ (black), $t = 0.3$ (red), $t = 0.6$ (orange) and $t = 0.9$ (pink). (b) Temporal evolution of the aspect ratio from left-hand side case. Both figures are in units of $2\eta = k_c = \gamma = 1$.

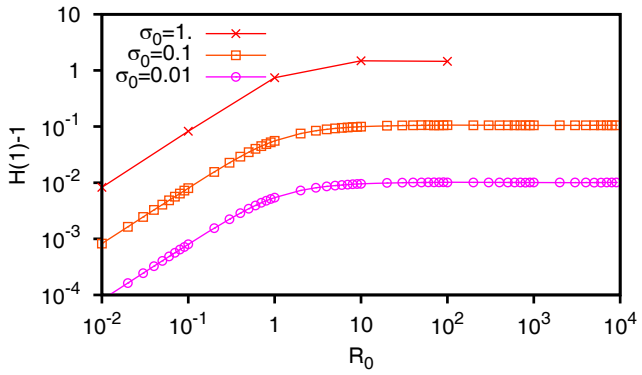


**Fig. 6.** Viscosity-dominated growth. Aspect ratio at the time point $t = 1$ as a function of the radius $R_0$ of the initial circular shape for different values of $\sigma_0$. The values are in units of $2\eta = k_c = \gamma = 1$.

the value of the initial radius of the circular tissue ($R_0$) compared to $L_c$, as shown in fig. 6. For $R_0 \gg L_c$, we recover the self-similar growth found in ref. [9]. On the contrary if $R_0 \ll L_c$, capillary effects act during a transient time estimated to be around $t \sim \log(L_c/R_0)/k_c$, inducing quasi-static deformations of the shape of the tissue. The aspect ratio grows then as $H(t) \sim \sigma_0 R(t)/\gamma$ as seen from eq. (9).

## 5 Model extensions

In our study we have omitted several effects and introduced simplifications for the sake of clarity of the analysis. Here we briefly discuss how the current scenario would be enriched or modified by the consideration of some of these additional effects.

An important restriction of our analysis is to assume that the rate of cell division and apoptosis does not vary across the tissue, in particular that is not affected by the local stress. This may not be justified in particular when stresses become large, resulting in some type of confinement of the growing regions to the appropriate boundary layers [23]. Inhomogeneous growth rates are certainly expected to affect the resulting morphology. In appendix G, we briefly discuss the problem near homeostatic conditions and we show that the circular tissue can reach a finite aspect ratio different from one at long times.

Another effect that could be introduced in the formalism is an anisotropy of the effective surface tension (*i.e.* $\gamma = \gamma_0 + \gamma_1(\mathbf{p}\cdot\hat{n})^2 > 0$) [24]. This could play a major role for small enough tissues and compete with the anisotropic cell division in defining the transient shapes of the growing tissue.

Regarding the dynamics of the cell polarization field, we have simplified the model by imposing that the axis of cell division is fixed by a spatially homogeneous external field. This is a justified assumption for instance in the growth of the imaginal disk of the fruit fly *Drosophila melanogaster* [9]. More generally, one could consider situations with a preferential cell orientation at the boundaries [25] or the reorientation of cell polarity by shear flow [26], which may be relevant in other contexts of tissue morphodynamics.

Finally, throughout this study we have mostly addressed the case of two-dimensional tissues. The case of three dimensions is qualitatively similar and is briefly discussed in appendix H.

## 6 Conclusion

We propose a hydrodynamic model to study tissue morphogenesis. In a polarized tissue, the orientation of cell divisions leads to the existence of anisotropic active stresses that drive ellipsoidal shapes. The aspect ratio of the shape has two qualitatively different behaviors depending on the dominant dissipative mechanism, either viscous or drag forces. A single length scale arises from the comparison between these two forces. For viscosity-dominated growth, the anisotropy builds up monotonically, whereas during friction-dominated growth, it decreases after a transient time of the order of the cell division time. Consequently, the aspect ratio in general shows a non-monotonic behavior, with a maximum at finite time, for which we give simple scaling laws which depend on the physical parameters of the tissue.

J.C. and C.B.-M. acknowledge financial support under the projects FIS2010-21924-C02-02 and 2009-SGR-014. C.B.-M also acknowledges a FPU grant from the Spanish Government, the Institute Curie and the exchange grant from the ESF Research Networking Programme QuanTissue. J.F.J. acknowledges support from the European network Mitosys.

## Appendix A. Dynamics of the area and the center of mass

In this section we calculate the dynamical equations for the area and the center of mass of a 2-dimensional tissue. Note that the argument can be generalized to 3-dimensional tissues. Both geometrical properties have their homologues in the harmonic moments formalism [27].

We start from the general result

$$\frac{\mathrm{d}}{\mathrm{d}t}\int_\Omega F(\mathbf{r})\mathrm{d}a = \int_{\partial\Omega} F(\mathbf{r})V_n\mathrm{d}l, \qquad (A.1)$$

$V_n$ being the normal component of the velocity of the interface (eq. (6)). We use the physical model of tissues given by eqs. (3), (4) where the tissue is on the domain ($\Omega$) and has a contour $\partial\Omega$. The time evolution of the total area is governed by the equation

$$\frac{\mathrm{d}A}{\mathrm{d}t} = \int_{\partial\Omega} V_n\mathrm{d}l = \int_\Omega \boldsymbol{\nabla}\cdot\mathbf{v}\mathrm{d}a = k_c A, \qquad (A.2)$$

where the left-hand side accounts for the mass produced per unit time. The center of mass position is defined in

vectorial notation by $A\mathbf{R}_A = \int_\Omega (x,y)\mathrm{d}a$. Considering first the $x$ component, we write

$$\frac{\mathrm{d}}{\mathrm{d}t}\int_\Omega x\mathrm{d}a = \int_{\partial\Omega} xV_n\mathrm{d}l = \int_\Omega \boldsymbol{\nabla}\cdot(x\mathbf{v})\,\mathrm{d}a, \tag{A.3}$$

$$= \frac{1}{\xi}\int_\Omega \boldsymbol{\nabla}\cdot\left(\sigma_{xx}^{\mathrm{tot}},\sigma_{xy}^{\mathrm{tot}}\right)\mathrm{d}a + k_c\int_\Omega x\mathrm{d}a, \tag{A.4}$$

$$= -\int_{\partial\Omega}\frac{\gamma}{\xi}\kappa\hat{n}_x\mathrm{d}l + k_c\int_\Omega x\mathrm{d}a, \tag{A.5}$$

$$= k_c\int_\Omega x\mathrm{d}a. \tag{A.6}$$

The same argument also holds for the $y$-component of the center of mass. The instantaneous velocity of the center of mass is thus

$$\dot{\mathbf{R}}_A = 0. \tag{A.7}$$

Since this result is exact for any shape of the tissue, we conclude that, within the assumptions of the model, the active stresses cannot drive a net displacement of the tissue. Note that this result is not trivial, because it is known that, in general, an active fluid in the presence of friction forces can indeed sustain motion provided that the shape of its boundary introduces an appropriate symmetry breaking [20].

## Appendix B. Self-similar growth

In this section, we review the particular case discussed in ref. [9] where there are neither friction nor capillary forces (*i.e.* $\gamma = \xi = 0$). Any initial shape evolves in a self-similar fashion. However, the scaling factors (along and perpendicular to the orientation of the cells) differ as long as the active stresses are finite, [9].

In the regime $\gamma = \xi = 0$, the tissue behaves as an incompressible Stokes flow with a free boundary. We assume that the polarization of the cells is homogenous across the tissue and parallel to the $x$-axis (*i.e.* $\mathbf{p} = \hat{e}_x$), and the dynamics of the interface is given by the kinematic condition (6).

The velocity field inside the tissue is given by $v_x = (k_c + \sigma_0/2\eta)x/2$, $v_y = (k_c - \sigma_0/2\eta)y/2$ and the pressure field is constant $P = \eta k_c - \sigma_0/2$, where $x$ and $y$ are the Cartesian coordinates. Importantly, this solution is independent of the instantaneous shape of the tissue.

We choose an arbitrary parametrization of a family of self-similar interfaces, $x = \lambda_x(t)x(s)$ and $y = \lambda_y(t)y(s)$, where $\lambda_y(t)$ ($\lambda_x(t)$) are the scaling factors in the $y$ and $x$ directions, respectively, and $(x(s), y(s))$ is a parametrization of the contour of the initial shape. Combining these results, the evolution of the initial contour is specified by two dynamical equations for the scaling factors $\dot{\lambda}_x = (k_c + \sigma_0/2\eta)\lambda_x/2$ and $\dot{\lambda}_y = (k_c - \sigma_0/2\eta)\lambda_y/2$, [9]. The original contour therefore deforms self-similarly.

One of the implications of this result is that a tissue would preserve a memory of its initial shape while growing. It is worth mentioning that one cannot eliminate completely this effect by invoking only capillary forces (*i.e.* $\gamma \neq 0$), because their effects are negligible at length scales larger than $L_c$.

## Appendix C. Linear perturbation analysis

We take as a starting point the reference solution of a circular shape with an instantaneous radius $R(t)$ in the absence of active stresses (*i.e.* $\sigma_0 = 0$), which is $\mathbf{v}_0 = k_c\mathbf{r}/2$ and $P_0 = -\xi k_c(r^2 - R(t)^2)/4 + \eta k_c + \gamma/R(t)$. We then assume that the amplitude of the active stresses $\sigma_0$ is finite but small, of order $\epsilon$. The active stress creates on the system perturbations of order $\sigma_0$. We express the new velocity and pressure field as $\mathbf{v} = \mathbf{v}_0 + \epsilon\delta\mathbf{v}$ and $P = P_0 + \epsilon\delta P$, where $\delta P$ and $\delta\mathbf{v}$ are the perturbation to the pressure and the velocity field, respectively. We limit ourselves to a determination of the shape of the tissue at linear order in $\epsilon$, so that the tissue becomes elliptical ($r(\theta,t) = R(t) + a_2(t)\cos(2\theta)$), where $a_2(t) \sim \mathcal{O}(\epsilon)$. In this case eqs. (3), (4) become

$$\eta\Delta\delta\mathbf{v} - \boldsymbol{\nabla}\delta P = \xi\delta\mathbf{v}, \tag{C.1}$$

$$\boldsymbol{\nabla}\cdot\delta\mathbf{v} = 0 \tag{C.2}$$

and the boundary conditions (5), (6) read

$$(\delta\sigma_{\alpha\beta}^{\mathrm{tot}} - (P_0 - \eta k_c)\delta_{\alpha\beta})\hat{n}_\beta|_{r=r(\theta,t)} = -\gamma\kappa\hat{n}_\alpha, \tag{C.3}$$

$$V_n = (\mathbf{v}_0 + \epsilon\delta\mathbf{v})\cdot\hat{n}|_{r=r(\theta,t)}, \tag{C.4}$$

where $\delta\sigma_{\alpha\beta}^{\mathrm{tot}} = \epsilon\eta(\partial_\alpha\delta v_\beta + \partial_\beta\delta v_\alpha) - \epsilon\delta P - \sigma_0 p_\alpha p_\beta$ is the perturbation to the total internal stress. We solved these equations using the computational software Mathematica. The interface dynamics at linear order in $\epsilon$, in terms of the instantaneous radius $R(t)$ and the aspect ratio $H(t) = 1 + 2a_2(t)/R(t) + \mathcal{O}(\epsilon^2)$ reads

$$\frac{\mathrm{d}R}{\mathrm{d}t} = \frac{k_c}{2}R, \tag{C.5}$$

$$\frac{\mathrm{d}H}{\mathrm{d}t} = -k_c\left(f_1\left(\frac{R}{L_\eta}\right) + \frac{L_c}{L_\eta}f_2\left(\frac{R}{L_\eta}\right)\right)(H-1) + \frac{\sigma_0}{\eta}f_3\left(\frac{R}{L_\eta}\right), \tag{C.6}$$

where the functions $f_i$, whose asymptotic behavior is discussed in the main text, are given here in units where $L_\eta = 1$:

$$f_1(R) = \frac{R^2\left(\left(R^2+8\right) - 4\left(R^2+4\right)\Pi(R)\right)}{((R^2+8)^2+32) - 4\left(R^2+6\right)\left(R^2+8\right)\Pi(R)},$$

$$f_2(R) = \frac{6}{R^3}f_1(R),$$

$$f_3(R) = \frac{4\left(\left(R^2+12\right) - \left(5R^2+24\right)\Pi(R)\right)}{((R^2+8)^2+32) - 4\left(R^2+6\right)\left(R^2+8\right)\Pi(R)},$$

where $\Pi(R) = I_1(R)/(RI_0(R))$, $I_1(R)$ and $I_0(R)$ being modified Bessel functions of the first kind [28].

## Appendix D. Conformal mapping formulation of the friction-dominated regime

The friction-dominated regime described in sect. 3 defines a new variant of the class of Laplacian growth problems in the context of the classical problem of viscous fingering in Hele-Shaw cells [29,30]. These free-boundary problems have in common a (usually two-dimensional) incompressible flow with a Laplacian velocity potential. The different interface dynamics is then determined by the distinct boundary conditions satisfied by the velocity potential at the interface. A similar example in a biological context has been recently discussed in ref. [20]. These problems can be formulated using conformal mapping techniques, which usually provide analytical insights and also a convenient numerical scheme that is competitive with other more general boundary-integral methods provided that the shape boundaries are not very contorted. Following refs. [27,29], in this appendix we derive an explicit interfacial dynamical equation in the friction-dominated limit (sect. 3) using conformal mapping techniques.

In the friction-dominated regime, the internal cell flow is approximated by an incompressible Darcy flow (11)-(12) complemented by the Young-Laplace condition at the interface (13). We redefine the pressure and velocity fields according to $P = \delta P - \xi k_c r^2/4$ and $\mathbf{v} = \delta\mathbf{v} + k_c\mathbf{r}/2$ such that the new fields $\delta\mathbf{v}$ and $\delta P$ satisfy the equations

$$-\boldsymbol{\nabla}\delta P = \xi\delta\mathbf{v}, \tag{D.1}$$

$$\boldsymbol{\nabla}\cdot\delta\mathbf{v} = 0, \tag{D.2}$$

that correspond exactly to the bulk equations of usual viscous fingering-like problems [29,30]. Therefore $\delta P$ is a Laplacian field. After this change of variables the kinematic boundary condition reads

$$\delta P|_{\partial\Omega} = \frac{\xi k_c r^2}{4} + \gamma\kappa - \sigma_0\hat{n}_x^2. \tag{D.3}$$

In this context, the contour of the interface can be described by a complex function $z = f(\phi, t)$ that maps the unit circle into the physical interface of our tissue, $\phi$ being the polar angle of the circle in the reference domain and $z = x + iy$ the complex coordinate in the physical domain. The second variable $t$ refers to time, to indicate that the interface shape evolves with time. The kinematic boundary condition in terms of this parametrization reads

$$\delta P|_{\partial\Omega} = \frac{\xi k_c|f|^2}{4} + \gamma\kappa[f] - \sigma_0\frac{Re[\partial_\phi f]^2}{|\partial_\phi f|^2}\,, \tag{D.4}$$

where $\kappa[f] = \mathrm{Im}[\partial_\phi^2 f\partial_\phi f^*]/|\partial_\phi f|^3$. The other interfacial quantities can be written in terms of the conformal mapping as

$$V_n = \frac{\mathrm{Im}[\partial_t f^*\partial_\phi f]}{|\partial_\phi f|}\,, \tag{D.5}$$

$$\delta\mathbf{v}\cdot\hat{n} + \frac{k_c}{2}\mathbf{r}\cdot\hat{n}|_{\partial\Omega} = -\frac{1}{\xi}\frac{\partial_\phi\delta\psi}{|\partial_\phi f|} + \frac{k_c}{2}\frac{\mathrm{Im}[f^*\partial_\phi f]}{|\partial_\phi f|}\,, \tag{D.6}$$

where $\delta\psi$ is the harmonic conjugate of $\delta P$.

Following refs. [27,29], $\delta\psi = \mathcal{H}_\phi[\delta P]$, where $\mathcal{H}_\phi$ is the Hilbert transform in the unit circle, defined as:

$$\mathcal{H}_\phi[\delta P] = \frac{1}{2\pi}P\int_0^{2\pi}\delta P(\phi', t)\cot(\phi - \phi')\mathrm{d}\phi'. \tag{D.7}$$

Therefore combining the previous results, one obtains the dynamic equation of the contour of the tissue (6):

$$\mathrm{Im}[\partial_t f^*\partial_\phi f] = \frac{k_c}{2}\mathrm{Im}[f^*\partial_\phi f]$$
$$-\partial_\phi\mathcal{H}_\phi\left[\frac{k_c|f|^2}{4} + \frac{\gamma}{\xi}\kappa[f] - \frac{\sigma_0}{\xi}\frac{\mathrm{Re}[\partial_\phi f]^2}{|\partial_\phi f|^2}\right]. \tag{D.8}$$

The numerical integration of the dynamics in this regime is based on this equation, which is reduced into a set of ordinary differential equations for the coefficients of the Taylor expansion of the analytical function $f(w, t)$, where $w = e^{i\phi}$.

## Appendix E. Exact stationary solutions in the friction-dominated regime

In this section we derive a class of exact stable solutions in the friction-dominated regime in the case where there is no tissue growth but in the presence of finite active stresses. These stationary solutions would correspond to situations where one can claim the existence of anisotropic active stresses that do not originate in cell division, but on other active processes of the cells. Even if the only active stresses are those of cell division, these solutions are still relevant to the dynamics as a sequence of shapes that the tissue is following quasi-statically, due to the fast relaxation of capillary forces (with a time scale ($\propto \xi R^3/\gamma$)) compared to the time scale of growth ($1/k_c$), so that $\xi R^3/\gamma \ll 1/k_c$. In this case, the radius can be considered as a slow variable that can be eliminated adiabatically. Remarkably, to the extent that the tissue dynamics can be considered to follow these shapes quasi-statically, the analysis of the morphology is not restricted to a small perturbation of the circle, since the solutions are exact. At this point it is worth stressing that such exact solutions in Laplacian-growth problems with a finite surface tension, where capillary forces can exactly cancel the corresponding driving forces of the problem, are very rare. The only two non-trivial situations where this has been shown to be possible so far in viscous fingering problems are reported in refs. [31,32]. Remarkably and contrary to those referred examples, our solutions are here linearly stable and therefore they are directly observable and play a relevant role in the dynamics.

Following the preceding examples, we start with an ansatz of exact mechanical equilibrium at the interface with zero flow, which reads

$$\gamma\kappa - \sigma_0\hat{n}_x^2 = P_0 = P_1 - \frac{\sigma_0}{2}\left(\hat{n}_x^2 + \hat{n}_y^2\right), \tag{E.1}$$

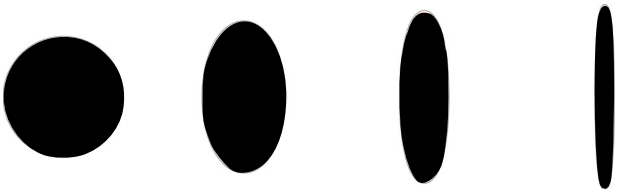

**Fig. 7.** Illustrative examples of exact stable solutions. The parameter $\alpha$ decreases from left to right. The shapes are oriented in the vertical axis for convenience.

where $P_0$ and $P_1$ are integration constants. The last equation is evaluated at the edge of the tissue. Parametrizing the contour with the arc length ($s$), eq. (E.1) becomes

$$\gamma\partial_s\Theta(s) - \frac{\sigma_0}{2}\cos\left(2\Theta(s)\right) = P_1, \tag{E.2}$$

where $\Theta(s)$ is the angle between the tangent vector at the interface and the axis of cell polarization, taken as the $x$-axis. The analytical solutions belong to the following family of uniparametric curves:

$$x(s) = \frac{L}{2\pi}\frac{\sqrt{\alpha+1}}{\sqrt{2}}\arctan\left(\frac{\sqrt{2}\cos\left(\frac{2\pi s}{L}\right)}{\sqrt{\alpha-\cos\left(\frac{4\pi s}{L}\right)}}\right), \tag{E.3}$$

$$y(s) = \frac{L}{2\pi}\frac{\sqrt{\alpha-1}}{\sqrt{2}}\operatorname{arctanh}\left(\frac{\sqrt{2}\sin\left(\frac{2\pi s}{L}\right)}{\sqrt{\alpha-\cos\left(\frac{4\pi s}{L}\right)}}\right), \tag{E.4}$$

$$\alpha^2 = 1 + \left(\frac{4\pi\gamma}{\sigma_0 L}\right)^2, \tag{E.5}$$

where $L$ is the perimeter of the contour. It is important to stress that in the absence of cell division, the area is a conserved geometrical quantity, and therefore the perimeter is a one-to-one function of the area. In fig. 7, we plot some examples of the previous solutions. The aspect ratio of a given solution of this family takes the form

$$H = \sqrt{\frac{\alpha+1}{\alpha-1}}\frac{\arctan\left(\frac{\sqrt{2}}{\sqrt{\alpha-1}}\right)}{\operatorname{arctanh}\left(\frac{\sqrt{2}}{\sqrt{\alpha+1}}\right)}. \tag{E.6}$$

Asymptotic behaviors of the aspect ratio can be found in the corresponding limits of small and large values of the dimensionless perimeter $\frac{\sigma_0 L}{\gamma}$,

$$H \sim \quad 1 + \tfrac{\sigma_0 L}{6\pi\gamma} \qquad \frac{\sigma_0 L}{\gamma} \ll 1, \tag{E.7}$$

$$H \sim \tfrac{\sigma_0 L}{4\gamma\log(\sigma_0 L/2\gamma)} \qquad \frac{\sigma_0 L}{\gamma} \gg 1. \tag{E.8}$$

Finally, we checked numerically that these solutions are generically stable to small perturbations.

## Appendix F. Conformal mapping formulation of the viscosity-dominated regime

Conformal mapping techniques can also be used to describe the evolution in the viscosity-dominated regime, in which the problem corresponds to a Stokes flow. In this section we derive the corresponding formulation, taking $\xi = 0$.

We first subtract from the physical fields the reference solution found in the absence of surface tension (appendix B) as $\mathbf{v} = \delta\mathbf{v} + (Ax, By)$ and $P = \delta P + C$ where $A \equiv (k_c + \sigma_0/2\eta)/2$ and $B \equiv (k_c - \sigma_0/2\eta)/2$ and $C \equiv \eta k_c - \sigma_0/2$. The original incompressible Stokes flows converts then into

$$\eta\Delta\delta\mathbf{v} - \boldsymbol{\nabla}\delta P = 0, \tag{F.1}$$

$$\boldsymbol{\nabla}\cdot\delta\mathbf{v} = 0. \tag{F.2}$$

These equations are formally equivalent to the hydrodynamic equations of a passive incompressible isotropic fluid. The boundary conditions are transformed into

$$\left(\eta\left(\partial_\alpha\delta v_\beta + \partial_\beta\delta v_\alpha\right) - \delta P\delta_{\alpha\beta}\right)\hat{n}_\beta|_{\partial\Omega} = -\gamma\kappa\hat{n}_\alpha, \tag{F.3}$$

$$V_n = \delta\mathbf{v}\cdot\hat{n} + (Ax, By)\cdot\hat{n}|_{\partial\Omega}. \tag{F.4}$$

We have thereby eliminated the active and anisotropic ingredients of the original equations. It is now possible to make use of conformal mapping techniques to solve these dynamical equations. For more details about the derivation, we refer the reader to the refs. [27,33].

The pressure field $\delta P$ is harmonic and the stream function $\delta\psi$ associated to the velocity field $\delta\mathbf{v}$ is biharmonic. We define the Airy stress function $\mathcal{A}$ as

$$-\delta P + \eta\left(\partial_x\delta v_x - \partial_y\delta v_y\right) = -2\eta\partial_y^2\mathcal{A}, \tag{F.5}$$

$$\eta\left(\partial_y\delta v_x + \partial_x\delta v_y\right) = 2\eta\partial_{xy}^2\mathcal{A}, \tag{F.6}$$

$$-\delta P + \eta\left(\partial_y\delta v_y - \partial_x\delta v_x\right) = -2\eta\partial_x^2\mathcal{A}, \tag{F.7}$$

which by construction is also a biharmonic function. Using the Goursat representation of biharmonic functions $\delta\psi$ and $\mathcal{A}$ may be expressed in the form

$$\mathcal{A} + i\delta\psi = -z^*\mu(z) - \chi(z), \tag{F.8}$$

where $z = x + iy$ is the complex coordinate, $x$ and $y$ being the Cartesian coordinates. The two functions, $\mu$ and $\chi$ are analytic functions. Using the Goursat representation and parametrizing the physical interface by a conformal mapping $z = f(\phi, t)$, that maps the contour of a unit circle into the physical interface, where $\phi$ is the polar angle of the circle in the reference domain and $z = x + iy$ the complex coordinate in the physical domain, we can rewrite the stress free boundary conditions (F.3) as

$$z\overline{\frac{\mathrm{d}\mu}{\mathrm{d}z}} + \overline{\frac{\mathrm{d}\chi}{\mathrm{d}z}} + \mu + \mathcal{G}(\phi)|_{z=f(\phi,t)} = 0, \tag{F.9}$$

$$\mathcal{G}(\phi) = \frac{\gamma}{2\eta}\int^{\phi}\kappa[f(\phi',t)]\partial_{\phi'}f(\phi',t)\mathrm{d}\phi' \tag{F.10}$$

and the kinematic boundary condition (F.4) as

$$\mathrm{Im}[\partial_t f^*\partial_\phi f] = -\mathrm{Im}[(2\mu + \mathcal{G})\,\partial_\phi f^*] + \mathrm{Im}\left[\frac{f}{2}\left(\frac{\sigma_0}{2\eta}\partial_\phi f - k_c\partial_\phi f^*\right)\right], \tag{F.11}$$

where $\kappa[f] = \mathrm{Im}[\partial_\phi^2 f\partial_\phi f^*]/|\partial_\phi f|^3$. We used these equations to solve numerically the time-evolution of the tissue shapes, such as those shown in fig. 5.

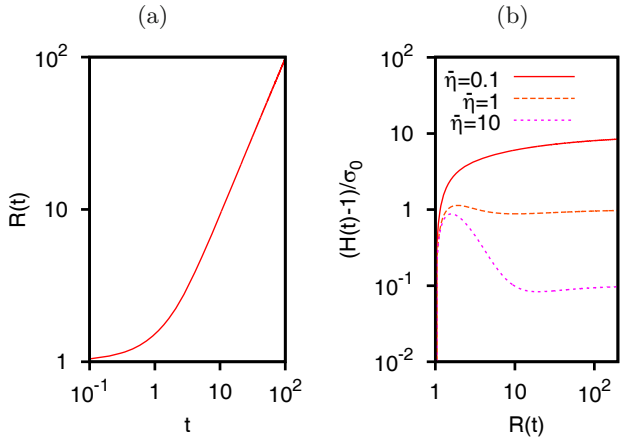


**Fig. 8.** (a) Dynamical evolution of the radius (eq. (G.1)) of an initially circular tissue for $\bar{\eta} = 100$. (b) Dynamical evolution of the aspect ratio (eq. (G.2)) against the instantaneous radius with a circular tissue as an initial condition. Both figures are in units of $R_0 = \xi = k_c = 1$.

## Appendix G. Tissue growth near the homeostatic state

In this section we briefly discuss the morphodynamics of a tissue that grows close to the homeostatic state with respect to the physical picture presented in the rest of this article. The discussion is limited to the friction-dominated regime and for simplicity we neglect capillary effects. We consider here a case in which the mechanical environment of the cell affects the cell state. As a starting point we take the model given by eqs. (11)-(12) with the boundary condition $P|_{\partial\Omega} = -\sigma_0(\hat{n}_x^2 - \hat{n}_y^2)/2$ and the kinematic equation (6), except that now the growth rate depends on the local stress, as $k_c(P) = k_c - P/\bar{\eta} > 0$. The quantity $\bar{\eta}$ has units of a viscosity. Its order of magnitude is estimated to be $\bar{\eta} \sim 10^9\,\mathrm{Pa\,s}$ for a spheroid composed of CT26 cells, [23], and the single characteristic length scale for this system is $L_{\bar{\eta}} \sim \sqrt{\bar{\eta}/\xi} \sim 1\,\mathrm{mm}$.

In the absence of active stresses (*i.e.* $\sigma_0 = 0$) a circular tissue spreads isotropically as shown in fig. 8. If $R(t) \ll L_{\bar{\eta}}$, we observe an exponential growth which suggests that $k_c(P)$ is roughly homogenous across the tissue, whereas if $R \gg L_{\bar{\eta}}$, then the radius increases linearly in time. This indicates that in the central region of the tissue, the division and death rates are balanced (homeostatic conditions) and thus only the cells at a distance of the order of $L_{\bar{\eta}}$ from the edge have a significant net proliferation rate.

On the other hand, the active stresses are anisotropically distributed along the edge of the tissue, as well as the growth rate $(k_c(P)|_{\partial\Omega} = k_c + \sigma_0(\hat{n}_x^2 - \hat{n}_y^2)/2\bar{\eta})$. In order to study the aspect ratio of the tissue, we performed a linear perturbation analysis considering $\sigma_0 \sim \mathcal{O}(\epsilon)$. The shape of the tissue deforms elliptically, $(r(\theta,t) = R(t) + a_2(t)\cos(2\theta))$, where $a_2(t) \sim \mathcal{O}(\epsilon)$. The aspect ratio is defined as $H(t) = 1 + 2a_2(t)/R(t) + \mathcal{O}(\epsilon^2)$. The dynamical equations obtained for $R(t)$ and $H(t)$ at linear order in $\epsilon$ are

$$\frac{\mathrm{d}R}{\mathrm{d}t} = k_c L_{\bar{\eta}} \frac{I_1(R/L_{\bar{\eta}})}{I_0(R/L_{\bar{\eta}})}, \tag{G.1}$$

$$\frac{\mathrm{d}H}{\mathrm{d}t} = -k_c \left( \frac{I_1(R/L_{\bar{\eta}})^2}{I_0(R/L_{\bar{\eta}}) I_2(R/L_{\bar{\eta}})} - 1 \right) (H-1) + \frac{\sigma_0}{\xi R^2} \left( -2 + \frac{R}{L_{\bar{\eta}}} \frac{I_1(R/L_{\bar{\eta}})}{I_2(R/L_{\bar{\eta}})} \right), \tag{G.2}$$

where $I_2(R/L_{\bar{\eta}})$, $I_1(R/L_{\bar{\eta}})$ and $I_0(R/L_{\bar{\eta}})$ modified Bessel functions of the first kind, [28].

Remarkably, the aspect ratio in the long time limit saturates to a finite value different from 1, as shown in fig. 8.

## Appendix H. Tissue growth in 3 dimensions

In this section, we justify that the global picture obtained in the friction-dominated regime (*i.e.* $R \gg L_\eta$) for 2-dimensional systems does not change qualitatively in 3 dimensions. As in the 2-dimensional case, we assume that the flows inside the tissue are described by a Darcy law for an incompressible fluid

$$\xi \mathbf{v} = -\boldsymbol{\nabla} P, \tag{H.1}$$

$$\boldsymbol{\nabla} \cdot \mathbf{v} = k_c, \tag{H.2}$$

combined with the boundary condition at the surface $\partial\Omega$

$$P|_{\partial\Omega} = \gamma\kappa - \sigma_0 \hat{n}_x^2, \tag{H.3}$$

where $\kappa$ is the total curvature in 3 dimensions. The $x$-axis is taken parallel to the preferential direction of cell orientation. The movement of the physical contour $\partial\Omega$ is defined by the kinematic equation $V_n = \mathbf{v} \cdot \hat{n}|_{\partial\Omega}$.

We base our analysis on the moment formalism generalized to 3-dimensional systems [27]. In general, we consider a function $L(\mathbf{r})$, such that $\nabla^2 L = 0$. Then

$$\frac{\mathrm{d}}{\mathrm{d}t} \int_\Omega L(\mathbf{r}) \mathrm{d}v = k_c \int_\Omega L(\mathbf{r}) \mathrm{d}v + \frac{\sigma_0}{\xi} \int_{\partial\Omega} \hat{n}_x^2 (\boldsymbol{\nabla} L) \cdot \hat{\mathbf{n}} \mathrm{d}a - \frac{\gamma}{\xi} \int_{\partial\Omega} \kappa (\boldsymbol{\nabla} L) \cdot \hat{\mathbf{n}} \mathrm{d}a. \tag{H.4}$$

We use this result for an ellipsoidal boundary $(x^2/a(t)^2 + (y^2+z^2)/b(t)^2 = 1)$, where $a(t)$ and $b(t)$ are the instantaneous semi-axes, and for the functions $L_0(\mathbf{r}) = 1$ and $L_2(\mathbf{r}) = x^2 - y^2$, whose integral over the physical domain $\Omega$ are related to the volume and the anisotropy of the shape respectively. For the sake of simplicity, we limit the discussion to shapes close to spheres, and so the aspect ratio $H(t) - 1 = \mathcal{O}(\epsilon)$, where $\epsilon \ll 1$. We obtain

$$\frac{\mathrm{d}R}{\mathrm{d}t} = \frac{k_c}{3} R, \tag{H.5}$$

$$\frac{\mathrm{d}H}{\mathrm{d}t} = -\left( \frac{2k_c}{3} + \frac{4\gamma}{\xi R^3} \right) (H-1) + \frac{2\sigma_0}{\xi k_c R^2}. \tag{H.6}$$

These equations are very similar to eqs. (8)-(10) so that the scaling laws found in the friction regime for 2-dimensional system remain valid in 3 dimensions.

## References


1. L. LeGoff, H. Rouault, T. Lecuit, Development **140**, 4051 (2013).
2. P. Campinho, M. Behrndt, J. Ranft, T. Risler, N. Minc, C.P. Heisenberg, Nat. Cell Biol. **15**, 1405 (2013).
3. T. Lecuit, L. Le Goff, Nature **450**, 189 (2007).
4. D.M. Bryant, K.E. Mostov, Nat. Rev. Mol. Cell Biol. **9**, 887 (2008).
5. S. Tlili, C. Gay, F. Graner, P. Marcq, F. Molino, P. Saramito, arXiv:1309.7432 (2013).
6. Y.K. Murugesan, D. Pasini, A.D. Rey, Soft Matter **7**, 7078 (2011).
7. F. Corson, O. Hamant, S. Bohn, J. Traas, A. Boudaoud, Y. Couder, Proc. Natl. Acad. Sci. U.S.A. **106**, 8453 (2009).
8. S.H. Tindemans, R.J. Hawkins, B.M. Mulder, Phys. Rev. Lett. **104**, 058103 (2010).
9. T. Bittig, O. Wartlick, M. González-Gaitán, F. Jülicher, Eur. Phys. J. E **30**, 93 (2009).
10. J. Ranft, M. Basan, J. Elgeti, J.F. Joanny, J. Prost, F. Jülicher, Proc. Natl. Acad. Sci. U.S.A. **107**, 20863 (2010).
11. E.K. Rodriguez, A. Hoger, A. D. McCulloch, J. Biomech. **27**, 455 (1994).
12. M. Ben Amar, A. Goriely, J. Mech. Phys. Solids **53**, 2284 (2005).
13. M.H. Köpf, L.M. Pismen, Soft Matter **9**, 3727 (2013).
14. T. Bittig, O. Wartlick, A. Kicheva, M. González-Gaitán, F. Jülicher, New J. Phys. **10**, 063001 (2008).
15. P. Kollmannsberger, C.M. Bidan, J.W.C. Dunlop, P. Fratzl, Soft Matter **7**, 9549 (2011).
16. F. Jülicher, K. Kruse, J. Prost, J.F. Joanny, Phys. Rep. **449**, 3 (2007).
17. M.C. Marchetti, J.F. Joanny, S. Ramaswamy, T.B. Liverpool, J. Prost, M. Rao, R.A. Simha, Rev. Mod. Phys. **85**, 1143 (2013).
18. J. Ranft, J. Prost, F. Jülicher, J.F. Joanny, Eur. Phys. J. E **35**, 1 (2012).
19. R.A. Foty, G. Forgacs, C.M. Pfleger, M.S. Steinberg, Phys. Rev. Lett. **72**, 2298 (1994).
20. C. Blanch-Mercader, J. Casademunt, Phys. Rev. Lett. **110**, 078102 (2013).
21. M. Basan, J.F. Joanny, J. Prost, T. Risler, Phys. Rev. Lett. **106**, 158101 (2011).
22. P. Lee, C.W. Wolgemuth, PLoS Comput. Biol. **7**, e1002007 (2011).
23. F. Montel, M. Delarue, J. Elgeti, L. Malaquin, M. Basan, T. Risler, B. Cabane, D. Vignjevic, J. Prost, G. Cappello, J.F. Joanny, Phys. Rev. Lett. **107**, 188102 (2011).
24. C. Godrèche, *Solids far from Equilibrium*, Vol. **1** (Cambridge University Press, 1991).
25. M.L. Manning, R.A. Foty, M.S. Steinberg, E.M. Schoetz, Proc. Natl. Acad. Sci. U.S.A. **107**, 12517 (2010).
26. B. Aigouy, R. Farhadifar, D.B. Staple, A. Sagner, J.C. Röper, F. Jülicher, S. Eaton, Cell **142**, 773 (2010).
27. L.J. Cummings, S.D. Howison, J.R. King, Eur. J. Appl. Math. **10**, 635 (1999).
28. M. Abramowitz, I.A. Stegun, *Handbook of Mathematical Functions with Formulas, Graphs, and Mathematical Tables*, Vol. **55** (Dover Publications, 1964).
29. D. Bensimon, L.P. Kadanoff, S. Liang, B.I. Shraiman, C. Tang, Rev. Mod. Phys. **58**, 977 (1986).
30. J. Casademunt, Chaos **14**, 809 (2004).
31. E. Álvarez-Lacalle, J. Ortín, J. Casademunt, Phys. Rev. Lett. **92**, 054501 (2004).
32. S.A. Lira, J.A. Miranda, R.M. Oliveira, Phys. Rev. E **82**, 036318 (2010).
33. L.J. Cummings, S.D. Howison, J.R. King, Phys. Fluids **9**, 477 (1997).